In-Situ Spatial Mapping of Hydrogen in Yttrium Hydrides at LANSCE

Alexander M. Long, James R. Torres, D. Travis Carver, Cristina G. Cardona, Erik P. Luther, Aditya P. Shivprasad, Caitlin A. Taylor, Holly R. Trellue, and Sven C. Vogel

LA-UR-22-29025
August 2022

Derivative Classifier Review
Reviewed and determined to be UNCLASSIFIED. This review does not constitute clearance for public release.
Derivative Classifier
Name/Z#/Org: Holly Trellue, 117909, NEN-5
Signature/Date:
Derived from: _

Prepared for: U.S. Department of Energy
Micro-reactor Program (MRP)
Holly Trellue, Technology Maturation Technical Area Lead
Systems Design and Analysis (NEN-5), LANL

Prepared by: Alexander M. Long and James R. Torres
Materials Science in Radiation and Dynamics Extremes (MST-8)

Approvals:

Name	Title	Signature	Date

Contents

Figures

Contents

Tables

Executive Summary

This report summarizes the neutron imaging techniques and experimental activities performed at the Los Alamos Neutron Science Center (LANSCE) with the main goal of measuring temperature-driven hydrogen diffusion within bulk-yttrium hydride (YH_x) materials. The experimental results and technique developments reported herein support the US Department of Energy Office of Nuclear Energy's (DOE-NE) Microreactor Program under Technology Maturation. In particular, the critical need to experimentally validate and verify hydrogen-diffusion models of metal hydrides used in high-temperature microreactor designs is addressed by means of high-spatial-resolution neutron imaging coupled with custom-built and application-specific furnaces. These capabilities were designed to apply large temperature gradients across centimeter-sized YH_x pellets to simulate conditions faced in the microreactor environment. Neutron imaging, combined with in-situ sample heating, enables near real-time tracking of hydrogen diffusion in YH_x on the sub-millimeter scale.

In this report, an overview of neutron imaging methodology and technologies are given in the context of recent spatial measures of hydrogen concentrations in similar metals hydrides. Additionally, the commissioning and operation of a custom-built compact dual-zone furnace is given along with details on the first two in-situ heating measurements of YH_x performed over the 2020 and 2021 LANSCE operation cycles. In parallel with in-situ heating measurements, neutron computed tomography scans were performed to visualize hydrogen aggregates in post-heated YH_x samples. Analysis and results from these neutron imaging measurements are given along with outlooks and plans for improving future hydrogen diffusion measurements at LANSCE.

Acronyms and Abbreviations

Acronym	Definition
ANP	Aircraft Nuclear Propulsion
CCD	Charge Coupled Device
CDZ	Compact Dual Zone furnace
CF	ConFlat vacuum connections
CT	Computed Tomography
DOE-NE	U.S Department of Energy Office of Nuclear Energy
EDS	Energy Dispersive X-ray Spectroscopy
ERNI	Energy Resolved Neutron Imaging
FOV	Field-of-view
FP5	Flight Path 5
FP11	Flight Path 11
HI	High-Intensity moderator
HIPPO	High-Pressure-Preferred Orientation diffractometer
HEU	High Enriched Uranium
KF	Kwik Fit vacuum connections
LANL	Los Alamos National Laboratory
LANSCE	Los Alamos Neutron Science Center
LEU	Low Enriched Uranium
MAUD	Material-Analysis-Using-Diffraction
MCP	Micro Channel Plates
ODF	Orientation Distribution Function
PID	Proportional-Integral-Derivative
RF	Radio-Frequency
SCICO	Scientific Computational Imaging Code
SEM	Scanning Electron Microscopy
SNAP	Systems for Nuclear Auxiliary Power
TMRS	Target-Moderator-Reflector-Shield assembly
TZM	Titanium-Zirconium-Molybdenum

1 Introduction

Microreactors are an emerging class of advanced, transportable nuclear reactors with the promise of providing power on the order of 0.1–20 MW to remote or hard-to-reach locations such as disaster-relief areas, military bases, and space systems. Given the transportable and remote nature of operations, new microreactor designs will require modular factory-like production, passively safe operations, compact self-contained form factors, and minimal maintenance and personnel requirements over its lifetime. With the goal to deploy the first prototypes within the next 5-10 years, the Department of Energy Office of Nuclear Energy (DOE-NE) Microreactor Program (MRP) aims to identify and bridge the technological gaps to meet design requirements. One of the overarching goals is to deliver a completely operational reactor on civilian transportation infrastructure. This prerequisite alone requires any microreactor design to be compact enough to fit on the back of a truck bed for transportation, while also requiring the use of low-enriched uranium (LEU), instead of high-enriched uranium, to minimize concerns for safety, security, and nuclear safeguarding.

To meet these design goals, new and advanced materials such as metal hydrides have been identified for microreactor moderator components, as the higher hydrogen density within the metal hydrides offer a higher moderating power and thus increased neutron absorption efficiency within the reactor core. Microreactors may potentially operate at temperatures higher than those at current commercial reactors for the purpose of achieving higher thermal efficiency [1]. Therefore, yttrium hydride (YH_x) is the leading moderator material candidate for several microreactor designs within the DOE-NE MRP and elsewhere due to its ability to retain hydrogen at very high temperatures relative to other metal hydrides. For example, with potential reactor operating temperatures in excess of 600 °C, hydrogen in yttrium hydride exhibits superior thermal stability over other metal hydrides such as zirconium hydride (ZrH_x), as illustrated in Fig. 1-1. By comparing hydrogen atom densities for various metal hydrides in Fig. 1-1, it is clearly illustrated that both zirconium and yttrium hydride retain the highest amount of hydrogen for temperatures above 500 °C. Moreover, comparisons between zirconium and yttrium hydride show that it onset of desorption in zirconium hydride occur at much lower temperatures than that of yttrium hydride.

The microreactor core is a dense composite of yttrium hydride moderator sandwiched between various heat sources and sinks. The anticipated temperature gradients across the moderator will drive hydrogen diffusion in a way that is not well understood and thus hinders design qualification and verification. For example, a key finding from the Systems for Nuclear Auxiliary Power (SNAP) and the Aircraft Nuclear Propulsion (ANP) programs was that strong hydrogen dissociation, migration, and diffusion effects were present in the metal hydride (ZrH_x) moderators [3], which negatively affected reactor performance. Hydrogen diffusion can be driven by various non-equilibrium transport processes, including Fickian diffusion (due to concentration gradients) and/or Soret diffusion (caused by a temperature gradient) [4]. As discussed in [4], Fickian and Soret diffusion present opposing effects, creating a feedback loop between the two processes until either a steady state is reached or the net hydrogen flux goes to zero. During this process, the diffusion of hydrogen through the hydride material can ultimately result in potential spatial stoichiometric variations within the moderator.

Currently, several computer models are being developed to better understand moderator behaviour of YH_x at various nominal and extreme reactor conditions, such as the code "Stoichiometry With Internally Fluctuating Temperature (SWIFT)" [5] as well as MCNP and Abaqus-based Reactor Multiphysics software (MARM) [4]. In order to validate these models, diffusion coefficients must be measured and verified experimentally. Moreover, in trying to capture off-normal opera-

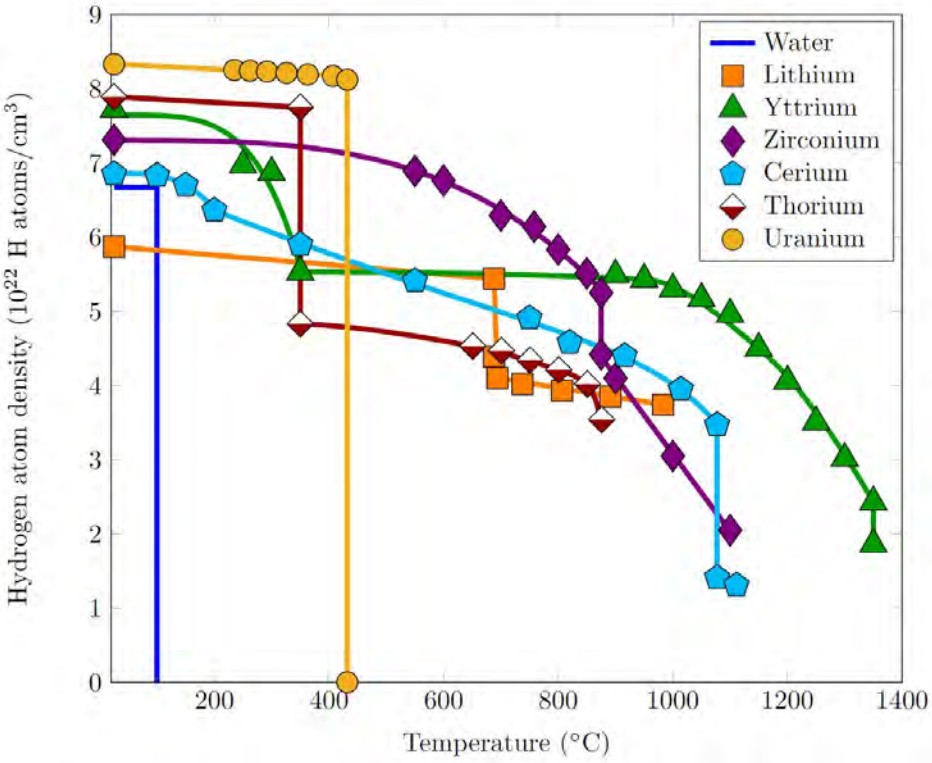

Figure 1-1: Atomic hydrogen densities, in equilibrium with 1 atm. of hydrogen gas, for various metal hydrides along with water for comparison. As temperatures increase, hydrogen within the metal hydrides becomes highly mobile and ultimately desorbs. Figure reproduced from [2]

tion behaviours, such as reactor start up or during an accident, understanding temperature-driven diffusion becomes most critical.

In this regard, significant investments have been made to build up neutron imaging capabilities at the Los Alamos Neutron Science Center (LANSCE) that characterize and measure temperature-driven hydrogen diffusion in YH_x. Here, neutron imaging offers the advantages of probing hydrogen movement in the interior of, and across, centimeter-sized YH_x samples both remotely and non-destructively; meaning that in-situ heating measurements can be performed with resulting 2D (and possibly 3D) maps of the corresponding hydrogen distributions. This presents an opportunity to induce temperature gradients across YH_x samples and measuring hydrogen distributions as a function of time and temperature to extract the valuable diffusion information.

1.1 Previous Work Using Neutron Imaging to Characterize Hydrogen in Metals

The application of neutron radiography to non-destructively characterize hydrogen concentrations in metal hydrides was first demonstrated by Klepeer *et al.* in 1968 for thin-walled, irradiated Zircaloy-2 tubing [6]. Using this method, it became clear that neutron radiography is a viable method to probe hydrogen concentrations with sensitivity resolution on the order of 500-1000 ppm wt.%, depending on the thickness of the Zircaloy samples. Since this first demonstration, neutron radiography techniques probing hydrogen concentrations in metal hydrides have steadily improved with implementations of modern digital imaging systems [7, 8, 9], calibrated samples [**Grosse2013**,

10, 11], and attenuation models [12] all of which were demonstrated in recent measurements by Buitrago *et al.* wherein energy-resolved neutron imaging at the pulsed-neutron source ISIS resulted in hydrogen concentration resolutions of 5 wt.% ppm [**Buitrago2018**]. While these measurements were made at ambient conditions, there have been recent developments in sample environments enabling in-situ heating measurements to investigate hydrogen uptake and diffusion in zirconium alloys (Zircaloys) [13]. Here, the samples were heated up to approximately 1750 K while exposed to an Ar/H_2 atmosphere in a custom-built furnace specifically made for in-situ neutron radiography. Following a calibration step where the relationship between neutron attenuation and hydrogen concentration per-pixel was established using pre-loaded hydrogenated samples, Fickian-like diffusion coefficients were determined from analysis of images of hydrogen diffusion fronts into Zircaloy-4 at various temperatures [13].

To date, most of the previous neutron imaging measurements on metal hydrides have been applied to zirconium metals and alloys. Given these successful demonstrations and reported results, this project aims to build similar neutron imaging capabilities at LANSCE to spatially map hydrogen concentrations in yttrium hydride samples, and potentially determine diffusion coefficients as a function of temperature and stoichiometry.

2 Setups and Methods

Hydrogen-mapping capabilities have steadily grown at LANSCE over the past three years, specifically on Flight Path 5 (FP5) and Flight Path 11 (FP11), in support of metal-hydride moderator research and development. This section covers sample preparation, furnace designs and implementations, neutron imaging flight paths, and recent measurements on YH_x samples, both ambient and at high temperatures, during the LANSCE 2021 run cycle. Additionally, measurements of YH_x and experimental setups on FP5 as performed during the 2020 LANSCE run cycle are described for completeness.

2.1 Sample Preparation

Samples were prepared by machining small cylindrical pellets from high-purity yttrium metal stock (Ames Laboratory, USA) and directly hydrided using established procedures [14, 15]. Yttrium metal was placed in a Sieverts-type apparatus consisting of an Inconel pressure vessel with the Y-metal placed on a molybdenum boat to prevent sample-vessel reactions. The vessel was evacuated to <1 Torr before heating up to approximately 820 °C. Hydriding was initiated by introducing approximately 10 Torr of hydrogen gas followed by additional small aliquots over time. During this process, the hydrogen flow rate was kept low (<40 Torr) to avoid cracking due to significant volume expansion encountered during hydriding. When the correct stoichiometry (H/Y ratio) was achieved, the sample temperature was lowered and the vessel evacuated to halt further hydrogen uptake. In total, five YH_x samples were made for hydrogen characterization measurements at LANSCE. Details on these samples are given in table 2-1.

Label	Stoichiometry (H/Y)[1]	Containment
176-1	1.899	Bare
172-2	1.906	Bare
178-1	1.919	Bare
157-2	1.628	TZM can
168-2	1.148	TZM can

Table 2-1: Information on all YH_x samples that were sent to LANSCE for neutron imaging measurements. After the hydriding process, all samples have similar geometries of approximately 5 mm diameter and 9 mm tall cylinders. The 157-2 and 168-1 samples were both loaded and sealed into a single TZM can under vacuum to prevent any oxidation during in-situ heating measurements.

The samples' dimensions were roughly 9 mm tall by 5 mm in diameter after hydriding. The containment used for the 157-2 and 168-2 YH_x pellets was a container (can) made of titanium-zirconium-molybdenum (TZM) alloy that was roughly 24 mm tall, 7.5 mm wide, and had a wall thickness of 0.25 mm. The two samples were loaded into a single TZM can and hermetically sealed under vacuum to prevent oxidation during heating. For all samples, their stoichiometries (H/Y ratios) were determined by weight gain after the hydriding process, whereas sample phase purity was confirmed through X-ray diffraction scans on identical witness sample from each hydriding batch.

[1] All stoichiometries were determined by weight gain after hydriding

Setups and Methods

2.2 Designing a Novel Furnace for In-situ Neutron Imaging Measurements

Detailed and quantitative investigations of hydrogen mapping in YH_x require high-spatial resolution neutron imaging and a novel furnace design - both made possible at LANSCE. The main requirements for this furnace were cast as follows: First, the geometry at the sample position must be as compact as possible with the a short sample-to-detector distance to reduce geometric-blur artifacts. Second, the furnace requires two independent heating elements that can sustain either uniform or gradient temperature profiles across samples up to several hundred degrees Celsius. Finally, the furnace must maintain a high-purity inert-gas atmosphere that prevents oxidation during heating. The so-called Compact Dual Zone (CDZ) furnace was thus designed in house specifically for such measurements (illustrated in Fig. 2-1a). With an outer tubing diameter of approximately 1", the CDZ furnace operated with minimal sample-to-detector distance that mitigates image blur and therefore resolution degradation. Additionally, heat transfer from the sample to the imaging detector was minimized by using quartz tubing with low thermal conductivity, inert gas flow within the furnace, and constant air cooling applied to the detector.

As seen in Fig. 2-1a, the core of the CDZ furnace design consists of two large molybdenum platens acting as thermal masses in contact with the sample at two opposing ends. Capable of operating in two distinct modes, these platens are either heated using radio-frequency (RF) coils, as shown in Fig. 2-1b, or resistive heating elements as shown in Fig. 2-1c. While RF heating tends to reach very high temperatures (beyond those tested here), the uniformity of the applied heat is difficult to control during experiments. With resistive heating, however, fine temperature control is readily achievable for both uniform and gradient temperature profiles, but the maximum temperature that can be applied to the sample is much lower (this was tested to be roughly 1100 °C). Additionally, using custom made resistive heaters fabricated by Zircar Ceramics that were independently controlled, temperature gradients of up 200 °C/cm can be applied across centimeter-long samples within the furnace.

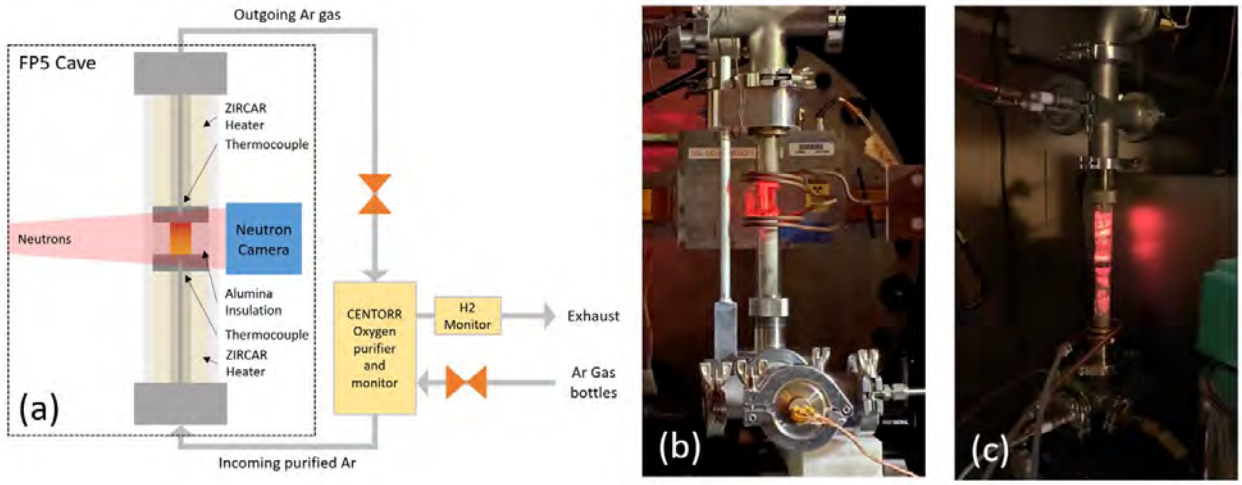

Figure 2-1: (a) Schematic of the CDZ furnace with resistive heating elements. Here, two molybdenum platens are potted inside Zircar ceramic heaters, which operate independently to create gradient or uniform temperature profiles across the samples. During heating operations temperature control is maintained by two thermocouples embedded in both of the molybdenum platens near the sample contact surface. Purified Ar cover gas prevents any oxidation of materials or samples. (b) The CDZ furnace operating in RF mode to apply uniform temperatures to YH_x samples in the 2020 measurements. (c) The CDZ furnace operating in resistive-heating mode to apply gradient temperatures to YH_x samples in 2021.

In order to prevent oxidation of materials and samples at elevated temperatures, a cover gas manifold system was built around a 2-Series Oxygen monitor and purifier from CENTORR Vacuum Industries. This manifold would allow for an argon cover gas to be purified before flowing through the furnace using a zirconium metal getter, while also monitoring the oxygen concentration in the exhaust once the argon exits the furnace. Additionally, a GD-70D gas sensor-transmitter from RKI Instruments, with a full-scale sensitivity of H2-500ppm/sec was inserted on the exhaust to monitor any hydrogen leaving the furnace.

For temperature control, thermocouples were embedded in the central axis of both the top and bottom molybdenum platens near the sample contact surface and connected to a Lakeshore-336 temperature controller. Once Proportional-Integral-Derivative (PID) parameters were calibrated, temperature resolution on the order of 0.1 °C was readily achievable with set-point temperatures up to 900 °C. The temperature stability of the furnace was found to work well over periods of hours to days during initial testing, and was able to hold large temperature gradients across surrogate steel samples for longer periods of time.

After two YH_x measurements on FP5, the CDZ furnace underwent several design iterations and upgrades, with further upgrades being implemented for the upcoming measurements during the 2022 LANSCE run cycle. Most recently, the CDZ furnace underwent a complete redesign in order to mitigate some of the oxygen incursion issues encountered during the latest experiment. The details of the redesign and upgrades are given in Sec. 4.1.

2.3 Neutron Imaging Beam Lines at LANSCE

FP5 and FP11 are both located at the Lujan Neutron Scattering Center (Lujan Center), an ISIS-class spallation neutron source at LANSCE [16]. Positioned on the lower tier of the Target-Moderator-Reflector-Shield (TMRS) assembly at the Lujan Center, FP5 views thermal to epi-thermal neutrons from a high-intensity, room-temperature water moderator, whereas FP11 views cold neutrons from a liquid-hydrogen moderator [17]. Specifications for both flight paths are given in table 2-2, while typical neutron flux as seen in nominal operations is shown in Fig. 2-2.

Flight Path Instrument	**E_n Range**	**Station Distance**	**L/D Resolution**	**Beam Dimensions**	**Integrated Flux (n/cm2 s)**
FP-11	0.5–20 meV	18–22 m	1000	6 cm × 6 cm	4.0x10^7
FP-5	25 meV–10 keV	7-11 m	100	8" diameter	4.0x10^7

Table 2-2: Neutron imaging flight path specifications for FP11 and FP5 at the Lujan Center. Values reproduced from [18]

From Fig. 2-2 it can be seen that the FP5 and FP11 flight paths are ideal platforms for visualizing hydrogen within metal hydrides as both have large fluxes in the thermal (FP5) or cold (FP11) neutron energy ranges where the hydrogen cross-sections dominate over the cross-sections of other isotopes like zirconium and yttrium.

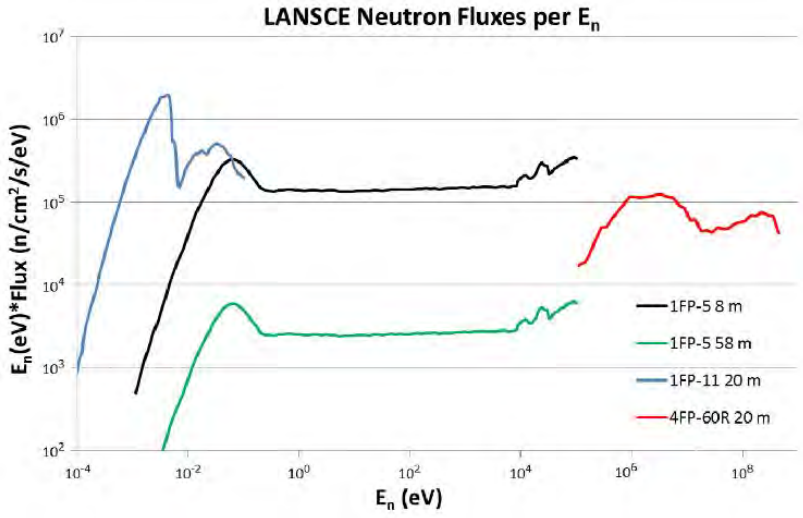

Figure 2-2: Neutron flux as a function of neutron energy for FP5 at a distance of 8 meters(black) and 60 meters (green) from the source, and FP11 at 20 meters (blue). Figure taken from [18]

2.4 In-situ Heating Measurements on FP5

Over the past two years, two separate in-situ heating measurements have been performed on FP5 with the goal of observing and characterizing hydrogen diffusion in YH_x samples. The first was performed during the 2020 LANSCE run cycle as a proof of principle measurement, while the second was performed during the 2021 LANSCE run cycle with the aim of measuring temperature driven hydrogen diffusion in a single bare-YH_x sample.

2.4.1 2020: Proof of principle measurements on FP5

Proof of principle measurements, with utilization of the first iteration of the CDZ furnace, were performed on FP5 during December of the LANSCE 2020 run cycle. A schematic of these measurements on FP5 are given in Fig. 2-3. On FP5, high-intensity pulsed neutrons stream out of the moderator of the TRMS [17] and down the flight path tube where the neutron beam is collimated down to a 2 cm diameter circular beam after exiting the flight path shutter. Located roughly 10m downstream of the moderator, the CDZ furnace, loaded with the YH_x samples, was positioned in front of a MCP-Timepix detector. With a slightly diverging beam, the beam spot size on the detector is slightly larger than 3 cm. The sample-to-detector distance was measured to be roughly 3.1 cm. The samples chosen for this first measurement were the $YH_{1.15}$ and $YH_{1.63}$ that were stacked on top of each other and sealed within a TMZ can.

The imaging detector used for these measurements was an MCP-Timepix camera constructed by Tremsin *et al.* [19, 20]. This ultra-fast imaging detector consists of two neutron-sensitive microchannel plates (MCPs), stacked in a chevron pattern, and coupled to four Timepix readout chips. Each readout chip contains an array of 256 x 256 pixels with a pixel-pitch of 55 μm, totaling to a 0.26MP sensor with a field-of-view (FOV) of 28mm x 28mm. With these Timepix readout chips, the detector setup is capable of producing images at frame rates above 60 kHz, or roughly 3000 frames per neutron pulse at the Lujan Center (which operates at 20Hz). Given that each frame has a timestamp with respect to the time-zero (T0) signal of the 1L target, neutron energies for each image

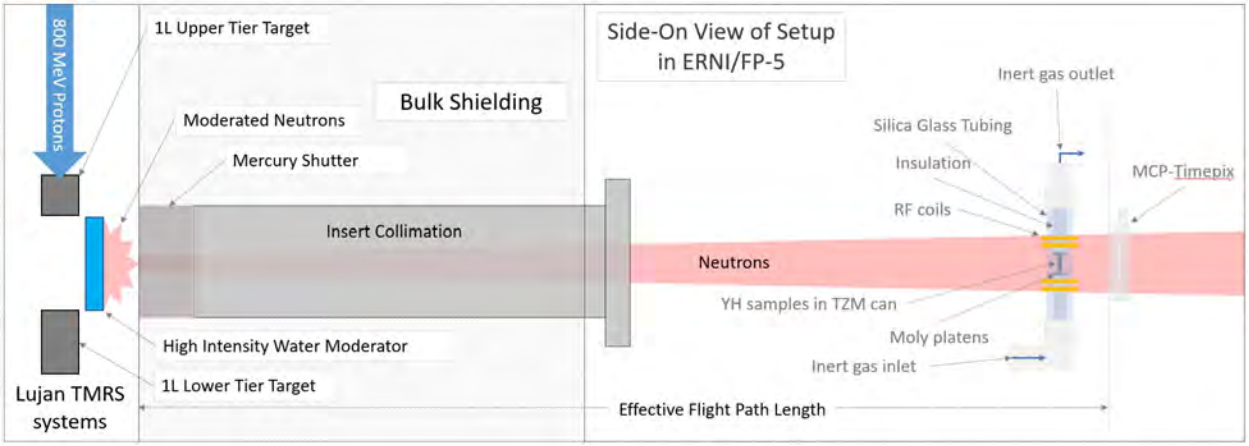

Figure 2-3: Setup for neutron radiography measurements on FP5 during the 2020 proof-of-principle measurements. Here, pulsed moderated neutrons stream out of the moderator and down the collimation of FP5. The samples, furnace, and imaging detector are located 10m downstream of the moderator.

can be determined by their time-of-flight along the fixed flight path lengths. Additionally, with the ability to configure the exposure shutters, certain neutron energies can be selected to create energy-specific contrast in a given neutron image. For these measurements, the MCP-Timepix camera shutters were configured to record 2461 images over a neutron energy range of approximately 10 meV to 1 eV, allowing for maximum contrast with the hydrogen within the YH_x samples as possible. A typical exposure time needed to accumulate enough statistics within a given image stack (in this configuration) was on the order of 15 to 30 minutes, depending on the source beam current.

Once the samples and container were placed inside the furnace, a 12-hour room-temperature exposure was recorded to understand baseline distributions of hydrogen within the sample. The final attenuation image at room temperature is shown on the right in Fig. 3-1. After the ambient-condition images were recorded, the furnace (in an RF configuration) was used to heat the samples with the following temperature profiles: 650°C, 750°C, 780°C, 800°C, 820°C, 840°C, 860°C, 880°C, 895°C, 750°C, 850°C, 825°C, 800°C, 775°C, 750°C. Six 30 minute exposures were recorded at each temperature, totalling to 3 hours per temperature. A selected few neutron attenuation images are shown on the left side of Fig. 3-1. Ramp rates between temperatures were set to 10°C per minute. The total beam time for the collection of all images, including ambient and open beam images, along with temperate ramping times, was roughly 55 hours. Given that the samples were sealed within the TMZ can, oxygen and hydrogen concentrations were not monitored for this measurement.

2.4.2 2021: Temperature driven diffusion measurements on FP5

Building upon the 2020 in-situ heating measurements with YH_x samples on FP5, modification were made to the in-situ heating setup such that hydrogen diffusion due to temperature gradients could be readily observed and possibly quantified. A schematic of the setup for the 2021 FP5 measurements are shown in Fig. 2-4. This setup was similar to the previous 2020 measurements, except for a few key changes. First, the CDZ furnace was modified to operate using resistive heating to allow for applied temperature gradients across samples. Second, the samples used for these measurements were not sealed in any containment, and instead bare YH_x samples were imaged. Finally, the MCP-Timepix detector was exchanged for a more traditional radiography setup with a Charge Coupled

Device (CCD) camera. Originally, 10 days of beam time were allocated to perform measurements on four YH_x samples, but unfortunately only a single in-situ measurement could only be performed on a YH_x sample (See 178-1 in Tab. 2-1) as the main power wires for the heating elements oxidized to the point of breaking and not enough parts were available at the time to repair the furnace to continue the additional measurements.

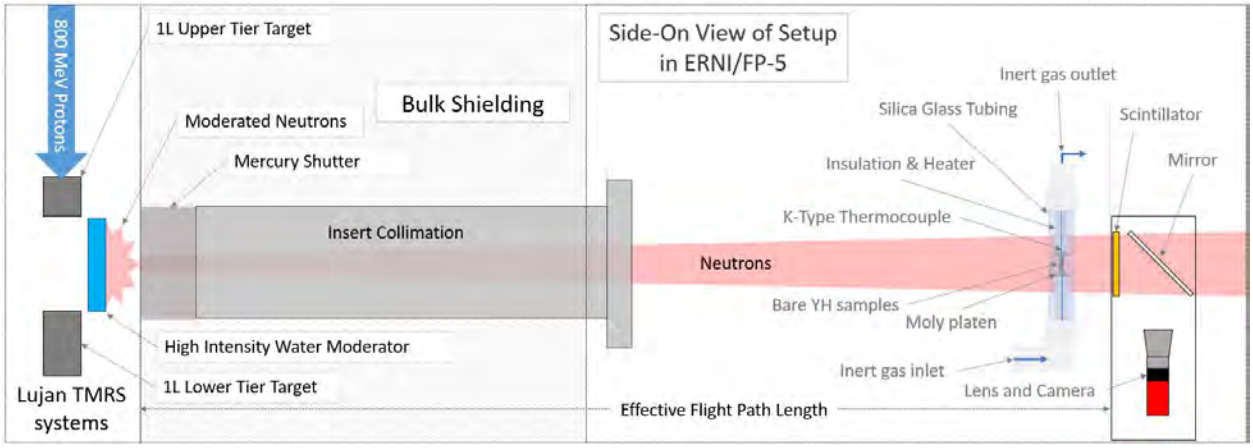

Figure 2-4: Setup for 2021 YH_x measurements on FP5. This setup was similar to the 2020 measurements, except that the CDZ modified to run with resistive heating, thus allowing for temperature gradients; and, a CCD camera was used instead of the MCP-Timepix detector, allowing for shorter exposure times on the order of minutes. Also, bare YH_x samples were used instead of samples sealed in a TZM container.

With the delivery of the Zircar Ceramics heating elements in the summer of 2021, the CDZ furnace could be outfitted to operate as intended with applied temperature gradients across single samples of YH_x. In order to ensure heat flow was directed along the vertical axis of the sample, the TZM can was removed, opting for bare-YH_x as the best path forward. In this case, the sample has good thermal contact with both top and bottom platens, and simple assumptions can be made between the temperature reading of the thermocouples and the actual temperature of the top and bottom of the sample. Additionally, alumina insulation was used to insulate the bare sample from potential cooling due to argon gas flow within the furnace. With the use of bare samples, oxygen and hydrogen monitors were utilized on the exhaust of the argon cover gas line of the CDZ furnace. Outputs of the oxygen and hydrogen monitors for the "178-1" in-situ heating measurements are shown in the bottom of Fig.2-5.

The thermal temperature profiles chosen for these measurements were similar to the ones used in the 2020 FP5 measurements, except that there is now a 50°C temperature gradient between the top and bottom of the sample. This is illustrated in the top of Fig.2-5, with the temperature profile that was recorded during the heating of the "178-1" sample. Here, neutron imaging measurements started at 300 °C and were incrementally increased to a maximum temperature of 900°C with alternating uniform and 50°C-gradient profiles. The temperature ramp rate was set for 10°C per minute. Each temperature change was held for approximately 30 minutes during which six 5-minute image exposures were taken of the sample. In total, the full in-situ measurement on the "178-1" sample, including the recording of open beam and dark images for analysis, took roughly 30 hours.

With the goal of reducing exposure times and capturing shorter hydrogen movement time scales, a traditional neutron radiography setup was selected for capturing neutron images in this particular setup. This consisted of a 200 μm Lithium doped zinc-sulfide scintillator screen (ZnS:LiF) from

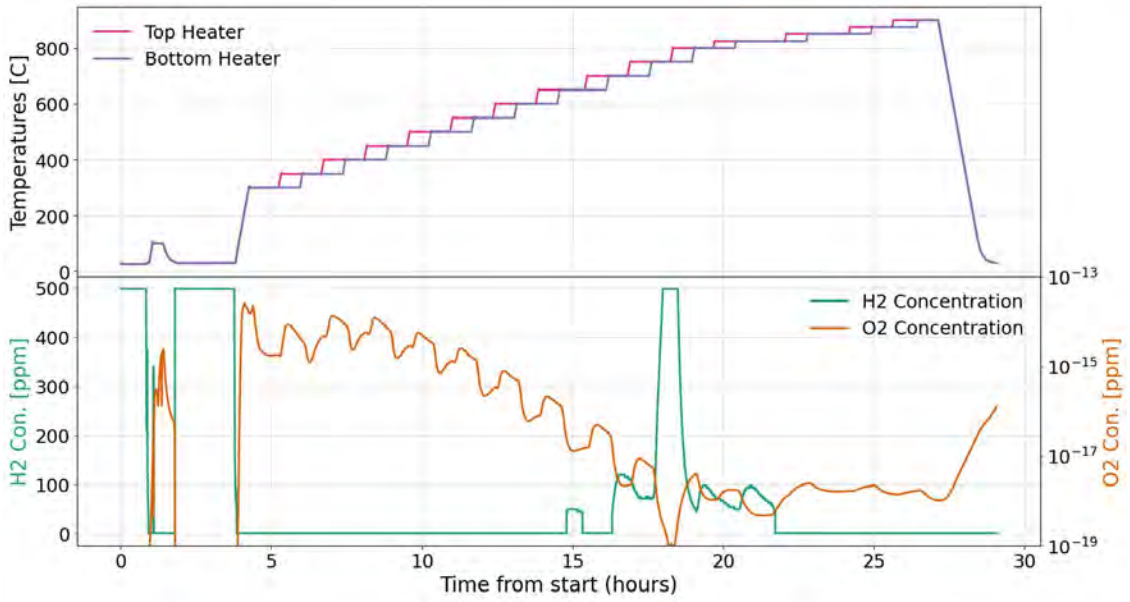

Figure 2-5: Top: Thermal profile for the in-situ gradient measurements on the "178-1" sample. Starting at 300°C, temperatures were increased by increments of 50°C, from 300°C to 900°C, with alternating uniform and gradient temperature profiles. Bottom: H_2 and O_2 concentrations as sampled in the exhaust of the CDZ furnace.

RCTretec coupled with a pellicle mirror, a Zeiss 50mm lens, and a ZWO-ASI 1600mm-Pro CCD camera. With this setup the optical resolution was determined to be around 35μm and the neutron resolution was found to be roughly 50um, which is due to the light spread in the ZnS:LiF scintillator. With this setup, exposure times needed to fill the dynamic range in contrast within neutron images was on the order of 5 minutes, depending on beam currents.

2.5 Ambient Neutron Imaging on FP11

After initial in-situ heating measurements were performed on the pair of YH_x samples at the end of the 2020 LANSCE cycle, additional measurements were needed to investigate the final distribution of the hydrogen with in the two samples. Utilizing the cold neutron imaging setup on FP11, neutron computed tomography (CT) was performed to better understand the final hydrogen distributions in the $YH_{1.15}$ and $YH_{1.63}$ samples. Neutron CT measurements on FP11 were performed using a traditional radiography setup similar to that on FP5. Here a 50 μm ZnS:LiF scintillator screen was used, which resulted in a neutron image resolution of roughly 25μm. The detector consisted of a Atik-490 EX monochrome CCD camera coupled with a 50mm Nikor lens. For the CT scan, a total of 360 neutron images were recorded over a full 360° sample rotation. Image exposure times were roughly 5 minutes per sample rotation, totalling to 30 hours for a full CT scan.

3 Analysis and Results

3.1 In-situ Heating Measurements of $YH_{1.1}$ and $YH_{1.6}$ Samples on FP5

The goal of this measurement was to utilize our neutron imaging techniques to observe hydrogen distributions in YH_x in the as-manufactured state as well as after H-redistribution at elevated temperatures. By obtaining accurate images that represent neutron attenuation lengths in each pixel, hydrogen densities distribution can be directly measured over the full area of the sample. For YH_x samples, the relationship between neutron attenuation lengths and hydrogen densities is given as,

$$\Sigma_{total} = N_H \sigma_H(n, tot) + N_Y \sigma_Y(n, tot), \tag{1}$$

where Σ_{total} is the total sum of neutron attenuation lengths, N_H and N_Y are the hydrogen and yttrium densities through the sample thickness along the beam path, and $\sigma_H(n, tot)$ and $\sigma_Y(n, tot)$ are the total microscopic neutron cross-sections for hydrogen and yttrium, respectively.

With neutron imaging, transmission images, $T(x, y)$, are obtained by taking an image of the sample, $I_{in}(x, y)$ and normalizing it to an image with the sample out of the beam ("open beam"), $I_{out}(x, y)$. A correction for background noise is made by subtracting a detector dark-current image taken with the beam off, $I_B(x, y)$. For energy resolve neutron imaging (ERNI), this is given as,

$$T(x, y, E_n) = \frac{I_{in}(x, y, E_n) - I_B(x, y, E_n)}{I_{out}(x, y, E_n) - I_B(x, y, E_n)} = exp\left(-\Sigma_{total}\ s(x, y)\right). \tag{2}$$

Here, $I_{in}(x, y, E_n)$, $I_{out}(x, y, E_n)$, and $I_B(x, y, E_n)$ are sample, open beam, and background images, respectively, as a function of pixel position (x, y) and neutron energy (E_n). Furthermore, neutron attenuation images, which include attenuation lengths Σ_{total} and the thickness of the sample $s(x, y)$, can be obtained by taking the negative logarithm of the transmission image, as seen in Eq. 2.

Nominally, neutron transmission and attenuation images can either be calibrated or modeled using the equations above to extract hydrogen density distributions. For these initial measurements, highly polished aluminum plates filled with water were initially used to calibrate hydrogen density to neutron transmission and attenuation. Though these calibration images were not used due to bubbles and other artifacts that prevented a clear analytical relationship. Instead, attenuation images were used to qualitatively assess hydrogen movement within samples as a function of temperature. A model-based approach was later used to quantify hydrogen concentration and is presented in Appendix A with some preliminary results.

After normalizing all $I_{out}(x, y, E_n)$ and $I_{in}(x, y, E_n)$ images to the proton beam current recorded by LANSCE facility using the Experimental Physics and Industry Control system (EPICS) [21], they were summed over all neutron energies (E_n) to enhance statistics and overall contrast quality. Using Eq. 2, neutron transmission and attenuation images were created for room temperature as well as each temperature within the heating profile. The final room-temperature neutron attenuation image is shown in Fig. 3-1, along with a head-on picture of the sample loaded in the CDZ furnace. Here, light-green and yellow colors represent high neutron attenuation (H-dense) whereas blue or purple represent little-to-no attenuation. Within this image, both $YH_{1.15}$ (top) and $YH_{1.63}$ (bottom) samples can be seen clearly within the TZM can, along with the two top and bottom platens. Additionally, a webbing structure within both the samples can be seen, which most likely represent hydrogen inhomogeneities with the samples. This structure later disperses once the samples are heated, thus casting little doubt that the higher attenuation regions within the sample are due to hydrogen aggregation.

Analysis and Results

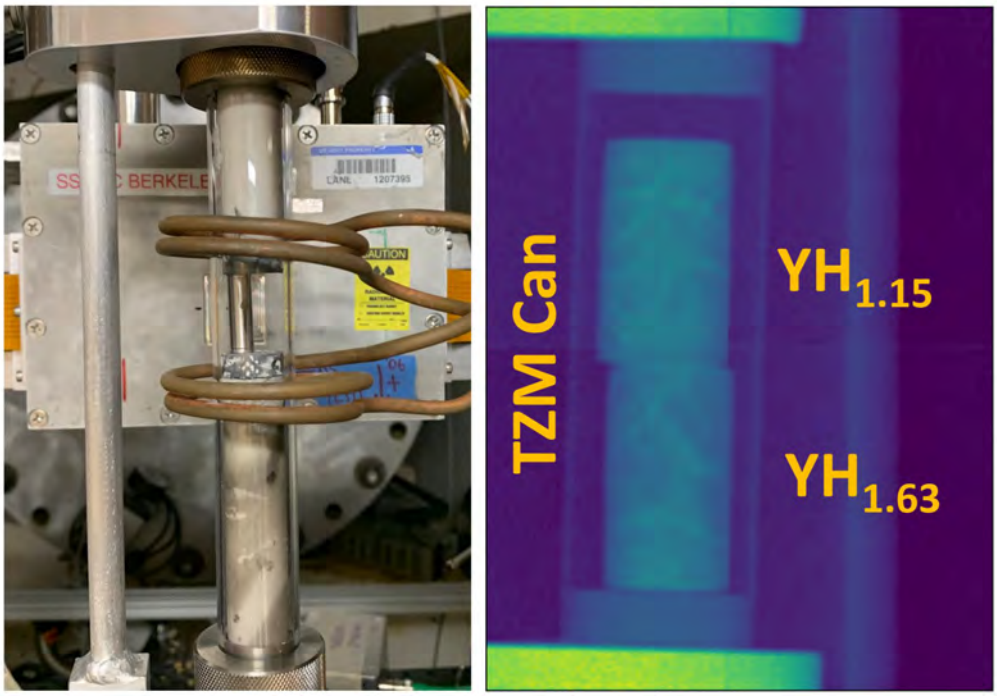

Figure 3-1: Left: Image taken of CDZ furnace with RF configuration and loaded with the TMZ can containing the $YH_{1.15}$ and $YH_{1.63}$ samples, along with the MCP-Timepix detector directly behind the furnace. Right: A neutron attenuation image taken at room temperature. The total exposure time was 12 hours. At room temperature, a webbing structure of hydrogen in both the $YH_{1.15}$ and $YH_{1.63}$ samples is easily observed.

Attenuation images of the $YH_{1.15}$ and $YH_{1.63}$ samples are shown in Fig. 3-2 for the various temperatures during the heating and cooling process. From this series of images, several key observations are made to understand hydrogen diffusion. First, the hydrogen webbing structure observed at room temperature persists up to approximately 800 °C, at which point the hydrogen mobilizes and appears to homogenize across both samples. This spatial uniformity appears as a constant uniform attenuation across both samples from 800°C to 860°C. Above 860°C, an attenuation gradient, and therefore a hydrogen gradient, appears within the samples with a strong downward orientation (more hydrogen at the bottom of the $YH_{1.63}$ sample). This hydrogen gradient continues to grow as the sample is heated up to 895°C and then cooled down to 700°C. After some initial analysis, it is proposed that the RF coupling to the bottom platen was not as strong as the coupling to the top platen. This in turn created a temperature gradient that would drive hydrogen to the cooler temperature regions within the sample container, which was at the very bottom of $YH_{1.63}$ sample. Additionally, this effect might have been exacerbated by the argon gas flow within the furnace, which flowed from the bottom up, and thus would affect the bottom platen and bottom of the TZM can disproportionally. Finally, as the samples cooled, a strong 3D-Gaussian-like distribution of hydrogen can be observed at the bottom of the $YH_{1.63}$ sample in the final attenuation image at 700 °C. Given that the actual temperature at the bottom sample is not strictly known, it becomes extremely difficult to understand the movement and final distribution of hydrogen without speculation for the temperature profile applied across the samples. Nevertheless, the observation of hydrogen movement within the samples via neutron imaging was the first of its kind with yttrium hydrides and shows promise provided certain corrections are made to the sample environment and furnace.

One of the key lessons from this set of measurements was the need for better sample environment designs with good thermal contact between sample surfaces and heating elements.

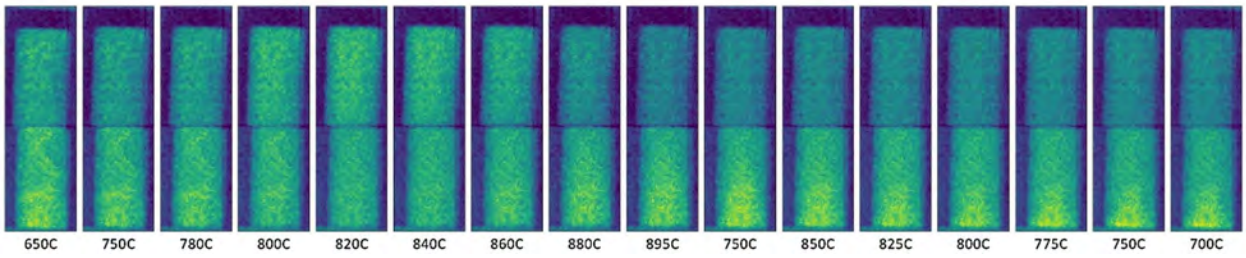

Figure 3-2: Neutron images taken as a function of temperature for two YH_x samples, $YH_{1.15}$ (top) and $YH_{1.63}$ (bottom). Samples were sealed within a TZM can thus preventing hydrogen from leaving the samples or surrounding container completely. Additionally, temperatures inside the TMZ can were not characterized.

3.2 In-situ Temperature Gradient Measurements of the $YH_{1.9}$ Sample on FP5

Given the successes and issues experienced with the 2020 measurement, several changes were made to the 2021 measurement plan on FP5. The main difference was the switch to a CCD camera instead of the MCP-Timepix detector, which means images were integrated over all neutron energies at each temperature profile for faster acquisition.

Similar to the 2020 measurements, in 2021 neutron images, $I_{in}(x, y)$, were taken for the $YH_{1.9}$ sample at room temperature and at elevated temperatures along with the sample out, $I_{out}(x, y)$, and background, $I_B(x, y)$. After images were normalized to the LANSCE accelerator beam current, neutron transmission and attenuation images were obtained according to Eq. 2. A final room temperature neutron attenuation image is shown in Fig. 3-3, along with a head-on image of the sample loaded into the furnace. Here, the sample is shown to have bright (yellow) contrast features translating to larger neutron attenuation from hydrogen. Additionally, the hydrogen distribution appears to be homogeneous throughout the sample, which is unsurprising for YH_x samples that are nearly stoichiometric, i.e., YH $_2$. The sample homogeneity was confirmed by spatially averaging the image pixel intensity along the vertical axis of the sample, which showed virtually the same intensity levels. This is in stark contrast to the $YH_{1.15}$ and $YH_{1.63}$, which showed large spatial variations in hydrogen distributions at room temperature.

Upon heating the sample from 300 °C to 900 °C, an interesting behavior was observed in the attenuation images where intensity levels within the sample increased linearly with temperature. Selected attenuation images are shown with adjusted high contrast in the top of Fig. 3-4. To verify this effect, spatially averaged intensity plots as a function of image sequence and temperature are shown in the bottom Fig. 3-4. It is well understood that as metal hydrides are heated to high temperatures, hydrogen will become mobile and eventually desorb until the partial pressures at the surface of, and around, the sample are equal. With hydrogen actively desorbing from the sample at elevated temperatures, a corresponding decrease in attenuation is expected since the macroscopic cross section decreases with hydrogen loss. Instead, a slow and constant *increase* in the attenuation is observed even at lower temperatures of roughly 400 °C. This behavior in the attenuation might be explained by oxidation of the sample during heating as was previously observed for zirconium cladding tubes subjected to systematic oxidation studies [12, 13]. Furthermore, oxygen concentration levels, as recorded by in the exhaust by an O_2 monitor depicted in Fig 2-5, show a

Analysis and Results

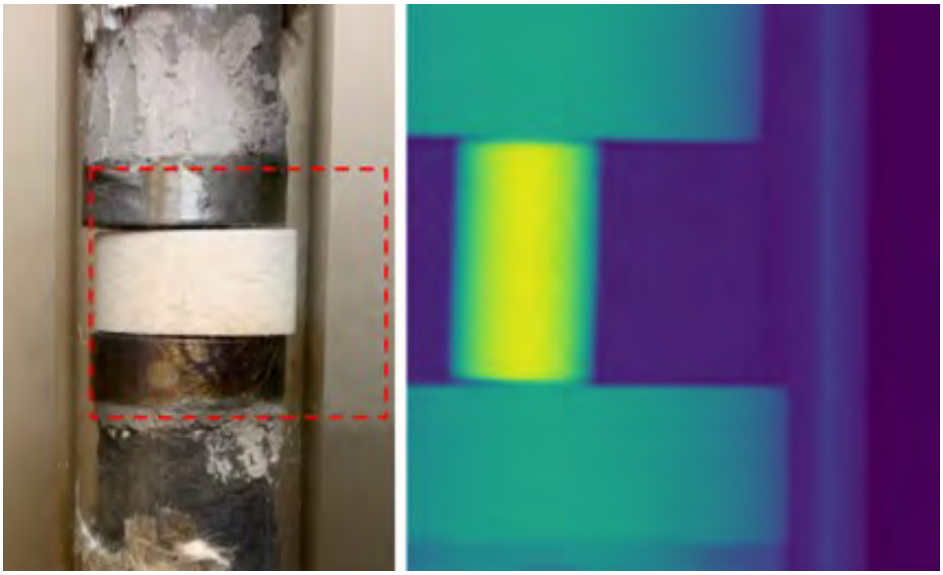

Figure 3-3: Left: Photograph taken of the $YH_{1.9}$ sample and insulation loaded into the CDZ furnace, the red-dotted box represents the image field of view. Right: Neutron attenuation image of the sample inside the CDZ furnace and adjusted for contrast, where high attenuation is represented as bright yellow, and low attenuation is dark blue.

significant decrease and therefore explained as oxygen uptake by the sample acting as an O_2 getter. We suspect the root cause is the Kwik Fit (KF) connections failing under heat and allowing small amounts of oxygen to be leak into the furnace and oxidizing the outer layers of the sample.

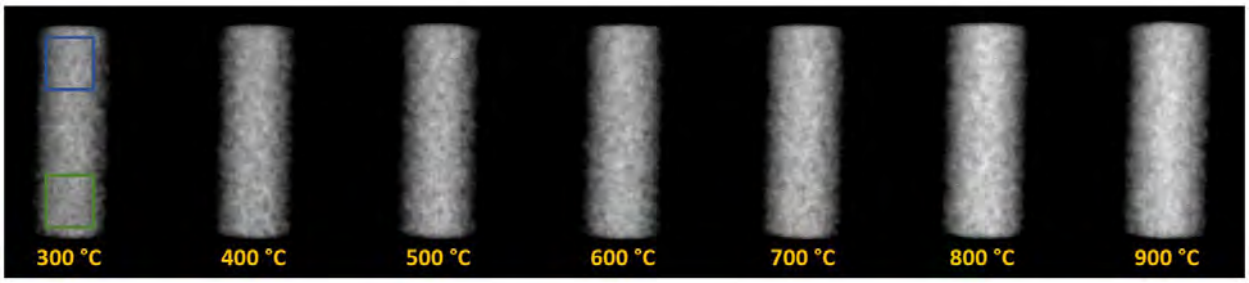

Figure 3-4: A series of selected neutron attenuation images as a function of temperature. Here, the temperature labels represent measurements performed with uniform temperatures, and the green and blue boxes illustrate regions of interest over which spatial averages are take of neutron attenuation.

Disassembly of the furnace after these imaging measurements revealed obvious sample oxidation by the color change from the as-received metallic dark blue to a grey-black oxide surface. In addition, there were fine grooves running azimuthally along the surface that were decorated with what looked to be particles from the alumina insulation. This is shown in a photo taken of the sample after heating in Fig. 3-6a. For completeness, a microstructural analysis of the $YH_{1.9}$ sample was performed using electron microscopy (SEM) to verify potential oxidation. The results are shown in Fig. 3-6b-c with scanning electron microscopy (SEM) images. Fig. 3-6b shows two levels of grey-scale contrast, the darker of which highlights the oxide film that grew along the sample surface as well as evidence of oxidation in the bulk. Additional elemental analysis of the sample surface via SEM energy dispersive spectroscopy-imaging in Figure 3-6c and 3-6d confirms the presence of an

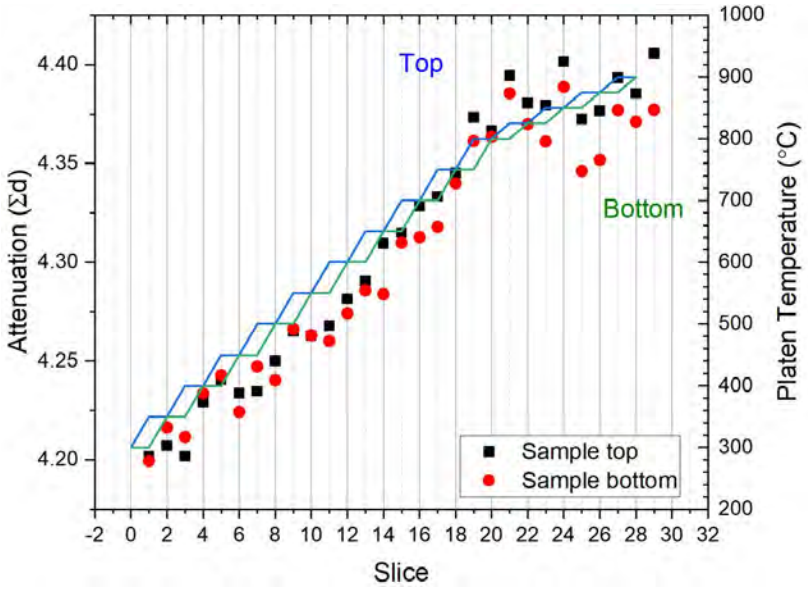

Figure 3-5: Plot of spatially averaged attenuation lengths and sample temperature versus image slice. Average attenuation lengths were taken over the blue (top sample) and green (bottom sample) regions highlighted above.

oxide. These SEM results confirm that sample experienced a significant amount of oxidation, most likely Y_2O_3, with build up on the surface and even inside the sample to some extent.

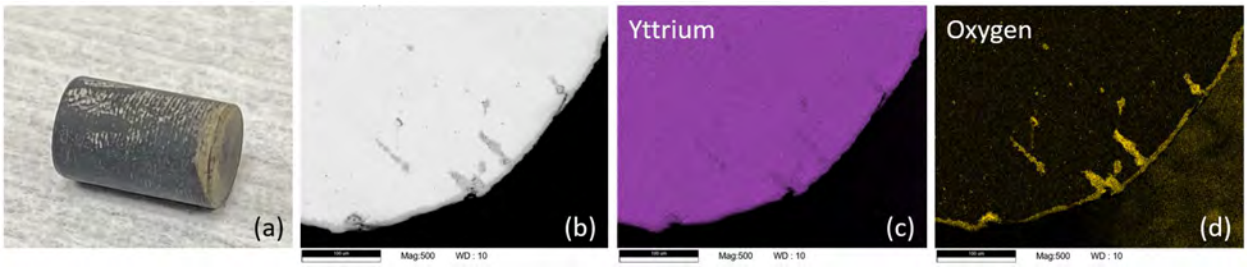

Figure 3-6: (a) Photograph taken of the $YH_{1.9}$ sample showing potential oxidation. Additionally, circumferential striping was observed on the sample, possibly coming from the alumina insulation used in the furnace. (b) Electron micrograph of sample cross-section that reveals oxidation contamination. (c)-(d) SEM elemental analysis of the yttrium and oxygen within the sample, respectively. Scale bars in all SEM images are 100 μm.

3.3 Neutron Imaging of post-heated $YH_{1.1}$ and $YH_{1.6}$ Samples on ASTERIX

As described above in Sec. 3.1, one of the main results of the 2020 in-situ measurement on FP5 was the observation of a Gaussian-like structure forming at the very bottom of the $YH_{1.63}$ sample during the cool-down phase after heating to roughly 895°C. This structure was not expected based on the temperature assumptions made during the measurements, and could only be explained if there was a faster cooling rate on the bottom of the sample container than on the top, which in turn resulted in an unintended temperature gradient on the two samples. As stated this could be explained possibly by a bottom-up cooling effect from the Ar cover gas flow or similarly a weaker RF coupling to the bottom platen.

Analysis and Results

To investigate this further, a full neutron-CT scan was performed on the sample on FP11. In total, 360 cold neutron radiographs ($I_{in}(x, y, \theta)$) were recorded over a full sample rotation of 360°. After recording images with sample out, $I_{out}(x, y)$, and background, $I_B(x, y)$, attenuation images were determined according to Eq. 2. With a full rotation set of attenuation images, a CT reconstruction of the samples was performed using the software *Muhrec* [22].

The results of this reconstruction are shown in Fig. 3-7. Fig. 3-7a shows an attenuation image taken at a given sample rotation, 3-7b shows a cross-sectional slice of the reconstruction with enhanced contrast, and 3-7c shows a 3D representation of the reconstruction using the program *Paraview* [23], where again contrast is enhanced to highlight the Gaussian-like structure. One of the key observations seen in this CT reconstruction is that this structure is not radially symmetric and is elongated in along one axis, illustrating that more complex temperature profiles might have been present.

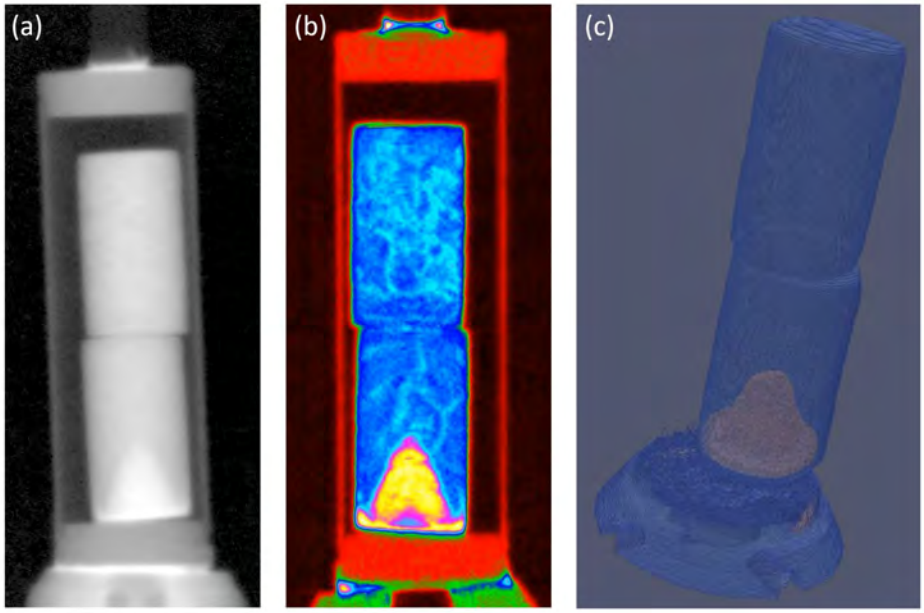

Figure 3-7: (a) Selected neutron attenuation image taken from CT scans performed on FP11. (b) Vertical cut of reconstruction samples at a given angle. The CT reconstruction was performed using the software *Muhrec*. (c) 3D representation of the two samples using the software *Paraview* with contrast tuned to highlight the large distribution of hydrogen at the bottom of the $YH_{1.63}$ sample.

4 Summary and Conculsions

To date, several measurements of imaging hydrogen distributions, both static and dynamic, have been performed using neutron imaging techniques on FP5 and FP11 at LANSCE. Initial proof-of-principle, in-situ heating measurements during that LANSCE 2020 run cycle proved successful in demonstrating that hydrogen movement within the YH_x samples could be observed at elevated temperatures. With RF heating, these measurements initially showed Fickian-like diffusion as the two samples with different stoichiometries ultimately reached equilibrium in their hydrogen concentrations and stoichiometries. Though as temperatures increased, hydrogen began to accumulate more and more in the bottom of the $YH_{1.63}$ sample, suggesting an unintended temperature gradient. Given that the actual temperatures of the samples inside the TMZ can were not well understood, and that many assumptions are needed to use the temperature reading on the top thermocouple, any diffusivity information could not be readily determined without speculation and perhaps extensive modeling.

With initial success and issues experienced from the 2020 in-situ measurements on FP5, the second set of in-situ measurements were designed with certain modifications to the sample and CDZ furnace. The first was the implementation of the Zircar heating elements into the CDZ furnace, which allowed for finely tuned temperature gradients to be applied across samples. The second was the exclusion of TZM cans that prevented good thermal contact with the top platen on the sample. Instead, bare YH_x samples were loaded into the furnace and an alumina insulation was used to surround the sample. This ultimately allowed for a better understanding of the applied temperature gradients across the samples; however, given the furnace connections of KF fittings, this setup allowed for oxygen leaks into the furnace during heating and thus readily oxidized the YH_x samples. This oxidation of the single $YH_{1.9}$ sample was later confirmed through electron microscopy analysis. Additionally, ambient-condition neutron-CT measurements were performed on FP11 to investigate the final hydrogen distributions of the two YH_x samples from the 2020 FP5 measurements. These results show that the Gaussian-like distribution of hydrogen with the $YH_{1.63}$ sample was non-symmetric and therefore alluded to a more complex temperature profile during heating and cooling while inside the furnace.

Moving forward, new measurements are planned for the 2022 LANSCE run cycle, both on FP5 and FP11, most likely starting in the October-November 2022 time frame. Additionally, new updates are being implemented with the CDZ furnace to allow for better oxygen mitigation during in-situ heating measurements. Finally, new sample containment designs are planned with the reuse of TZM cans along with tantalum wire that would allow for remote thermometry throughout the experiment.

4.1 Upgrades to CDZ Furnace and Redesign of TMZ containment

Given the issues with oxidation of samples with the older CDZ furnace design, new ConFlat (CF) seals with copper gaskets are being implemented and replacing all the original Kwik Flange (KF) connections. This will reduce the potential for oxygen leaks in the majority of the furnace connections. Additionally, the original quartz-tube assembly will be replaced with either a stainless-steel full CF flange, roughly 19" long, or ceramic tubing such as mullite ($SiO_2Al_2O_3$) or quartz(SiO_2) with bonded metal-CF flanges on either side. For reference, a photograph of the setup is given in Figure 4-1 with the 19" stainless steel CF tubing.

The furnace redesign also includes several auxiliary improvements. Namely, the bottled-argon

source gas will be replaced with liquid-argon boil-off coupled with both upstream and downstream gas monitoring to characterize gas purity. This will not only allow for potentially more pure argon gas on the furnace inlet (less oxygen), but the simultaneous monitoring in the upstream and downstream will allow for real time detection of oxygen leaks in the furnace. The addition of a linear motion device at the top of the furnace along with alumina baffles on the heaters (see Fig. 4-1 schematic) will enable easier and more reproducible sample positioning in the beam. Moreover, the linear motion device allows for variable sample height with a 50 mm stroke length. Finally, a 6-port CF cube at each side of the furnace allows for future expansion, including an array of thermocouples to better map the temperature profile anywhere in the furnace. We note that these additions will reduce the time needed to swap samples, leading to more efficient use of the planned beam time.

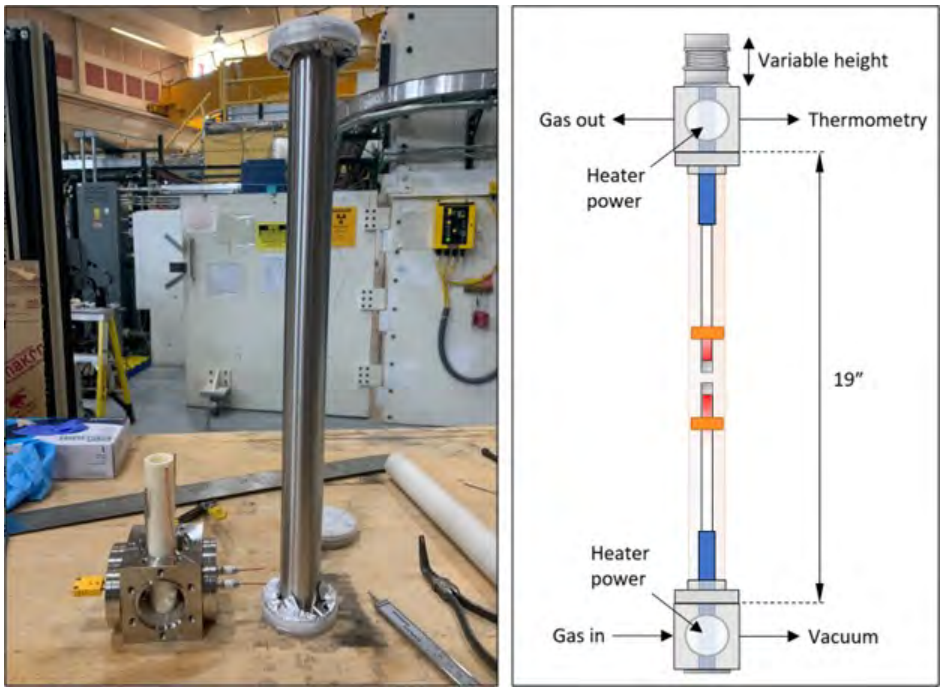

Figure 4-1: (left) Partial assemblies of the redesigned CDZ furnace with a stainless steel option of the main sample housing. (right) Schematic of the furnace layout. Here, all of the original fitting are replaced with CF flanges that are rated for much higher temperatures than KF connections.

In parallel with the current upgrades in the CDZ furnace, a new sample containment design with TMZ containers has been implemented to allow for better understanding of the true temperatures closest to the samples. More specifically, tantalum (Ta) wires have been included as wedges around and above the samples within the TZM container. These Ta wires serve two purposes. The first is to prevent any radial contact with the TMZ can and thus prevent non-axial heat flow to the sample. Second, neutron capture resonances within the Ta wires can be used to measure changes in temperature by measuring the Doppler broadening in any individual resonance. A schematic of the TZM container with the sample and Ta wires is shown in Fig. 4-2. With three wires running down the sides and a large Ta wire placed on top, a temperature profile can be mapped out remotely, relative to the bottom platen, using the changes observed in the broadening of the neutron capture resonances in Ta. With the use of this type of sample containment, oxidation is mitigated further and temperature profiles can be obtained remotely.

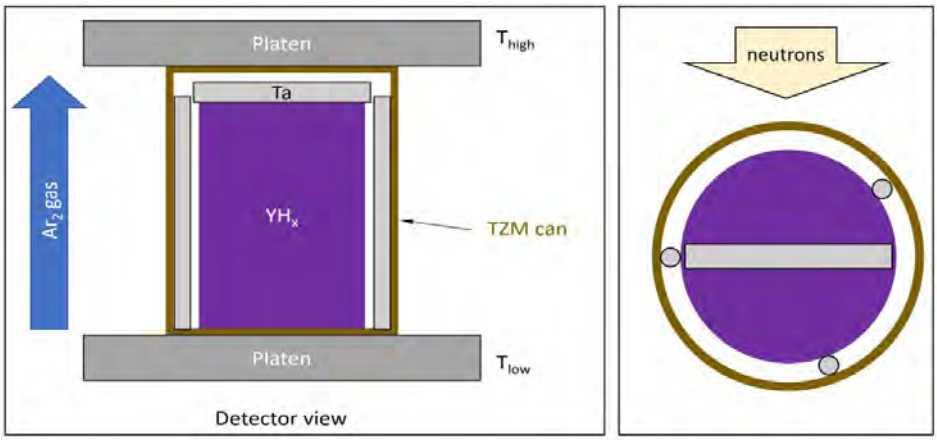

Figure 4-2: Schematic diagram of the current sample and container design. Here, samples will be loaded and sealed in TZM containers to help mitigate oxidation during heating. Additionally, Ta wires will be used as wedges around the sample to prevent any radial contact with the TZM container. These wires will enable remote temperature sensing of the sample to better understand the applied heating profiles.

The technique of using the Doppler broadening from neutron absorption resonances of Ta metal for remote temperature measurements was first demonstrated on FP5 in 2001 [24] and was later used in Energy Resolved Neutron Imaging (ERNI) to create a spatial map of temperatures in Ta foils [25]. Results from [25] are shown in Fig. 4-3 where the 4.26 eV and 10.3 eV resonances were imaged in a heated-Ta foil, 100 μm thick, using ERNI techniques, thus allowing for a spatial mapping of the applied temperature to the Ta foil within the detector's field of view. Building upon the success of this first measurement on FP5, adoption of this technique for future in-situ heating measurements on YH_x samples will help better understand temperature profiles along the vertical axis when using a TZM container. Essentially, good thermal contact between the top platen and the sample will no longer be needed as the thermocouple reading with the bottom platen and the profile of Doppler broaden resonances around the sample can be used to build an applied temperature profile during each in-situ heating measurement.

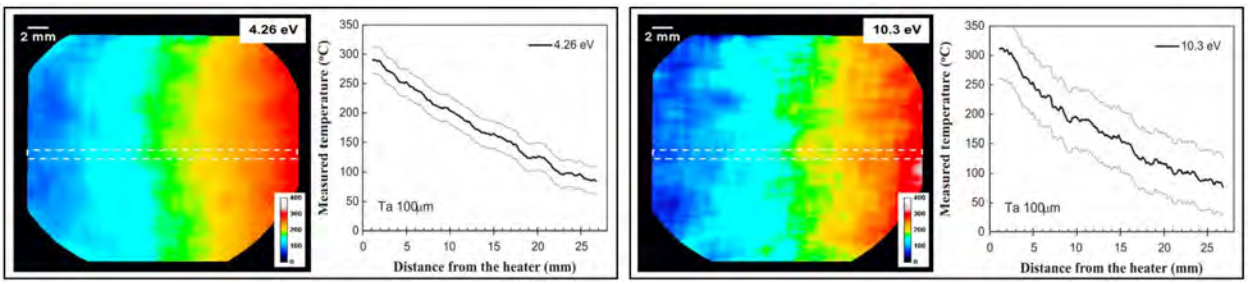

Figure 4-3: Remote temperature mapping of 100 μm-thick tantalum foils using the observed Doppler broadening of the 4.26 eV (right) and 10.3 eV (left) neutron capture resonances in ^{181}Ta. Figure modified from [25].

4.2 Planned 2022 LANSCE Run Cycle Measurements

With the described upgrades to the furnace and sample containment, several new sets of measurements are planned for the upcoming 2022 LANSCE run cycle. In total, 15 days of beam time on

Summary and Conculsions

FP5 have been granted by the LANSCE PAC, along with 10 days on FP11. Beam time on FP5 will be used for the main in-situ heating measurements, while beam time on FP11 will be used for pre- and post-characterization of 3D hydrogen distributions within the given sample set via neutron-CT scans. These CT scans will aid in better understanding the initial and final hydrogen distributions. In total, 10-15 samples with variation in their stoichiometries, original metal stock, and hydriding processes, have been identified for in-situ heating measurements on FP5. Additionally, 2-3 samples of interest have been identified based on computer simulations using SWIFT in collaboration with theorists [5].

Initial FP5 in-situ heating measurements will first utilize samples in TMZ containers to completely eliminate any oxidation effects with the samples. Given this choice, the MCP-Timepix detector will be used, allowing for ERNI measurements that capture the epi-thermal neutron flux for neutron capture resonances within the surrounding Ta wires, along with the thermal neutron flux that is most sensitive to the presence of hydrogen. Prior to in-situ heating measurements, several calibrations are required. The first will be to establish temperature dependence of the Doppler broadening of Ta wires of a given neutron absorption resonance. The second will be to use water calibration samples to allow for more reliable mapping between neutron attenuation and hydrogen density in each detector pixel. We note that if the Ta wire fails to remotely measure temperature, either being insensitive or ineffective, we will then turn to using bare samples with great care to monitor and mitigate oxygen incursions during heating.

In addition to neutron CT scans on FP11, neutron diffraction measurements on the HIPPO neutron diffractometer are planned to investigate micro-structure and phase fractions of the samples in the as-received state. Diffraction measurements on post-heated samples will be considered as well, time permitting. This proposed multifaceted approach will enable the most comprehensive understanding of macro-scale hydrogen mobility, along with both pre- and post-heating characterization, which is critical for better diffusion measurements and ultimately diffusion modeling.

Appendix A: Quantitave Analysis of Hydrogen in YH

In this section, neutron radiography data that was collected during in-situ heating of yttrium hydride solid state moderator pellets are analyzed in a quantitative way. The data correspond to an experiment where two moderator pellets with different initial compositions are vertically stacked and subjected to heating. The bottom pellet has a higher initial hydrogen composition ($YH_{1.6}$) while the top one was lower ($YH_{1.1}$). The heating profile consists of two stages: temperature increase and decrease. A number of images (16) were taken at temperature of 650°C, 750°C, 780°C, 800°C, 820°C, 840°C, 860°C, 880°C, 895°C, 750°C, 850°C, 825°C, 800°C, 775°C, 750°C and 700°C. Fig. A-1 displays these 16 snapshots where k corresponds to a temperature in the temperature sequence above.

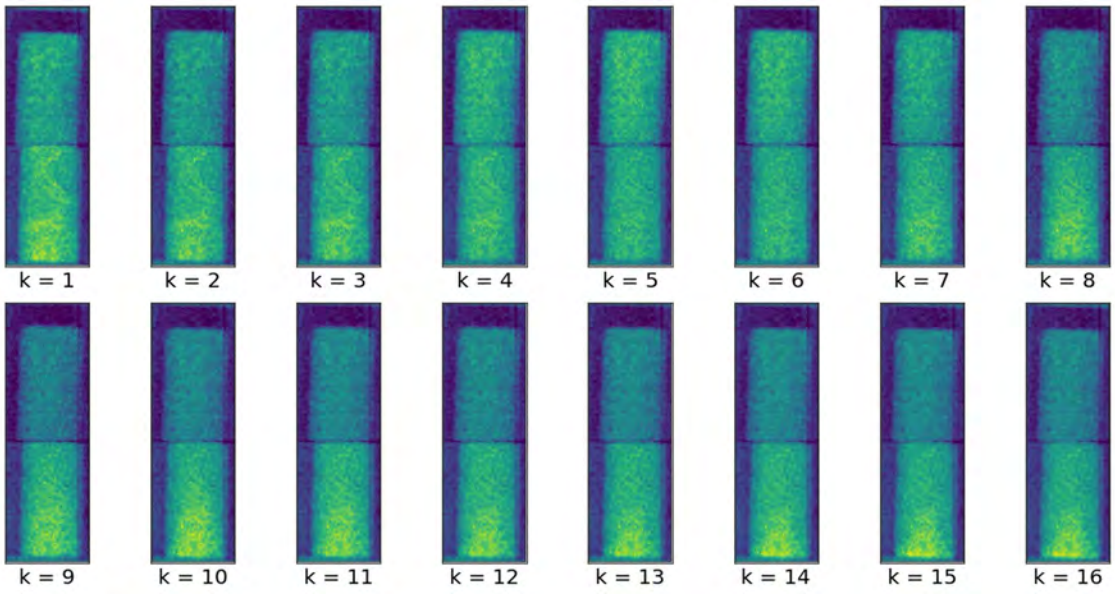

Figure A-1

To model and solve for hydrogen concentrations under this temperature gradient, neutron attenuation images were further processed in that contributions from the TMZ containment as well as the cylindrical geometry of the samples were corrected for by dividing out the $s(x, y)$ term in Eq. 2. The results represent images of true neutron attenuation lengths per unit thickness coming only from the YH_x samples. With these final images, a system of linear equations was constructed based on the physics of neutron attenuation from YH_x samples, specifically with hydrogen being able to move freely between pixels while the yttrium atoms remain static. The system of constructed equations then follow,

$$n(H)_{ijk}\sigma_H + n(Y)\sigma(Y) = p_{ijk} \tag{3}$$

$$\sum_{ij} \frac{n(H)_{ijk}}{n(Y)N} = C \tag{4}$$

where $n(H)_{ijk}$ is the areal concentration of hydrogen in each pixel (i, j), per snapshot k in atoms/mm^2, and $n(Y)$ is the areal concentration of yttrium. σ_H and σ_Y are the thermal averages of neutron

cross-sections of hydrogen and yttrium, respectively. p_{ijk} is the pixel intensity for each k snapshot. N is the number of pixels per snapshot k, and C is a constant representing global composition ratio, which is taken as the average of the two stoichiometries of $YH_{1.15}$ and $YH_{1.63}$. The first set of equations expresses the fact that for each snapshot k, the intensity measured for each pixel (i, j) should be the result of the (i, j) spatial composition of the pellet at snapshot k; this in turn corresponds to the cross-section for neutrons of each material multiplied by their areal concentration. Note that the yttrium concentration is constant throughout the stacking of pellets and throughout all the snapshots, while the hydrogen concentration varies spatially (i, j) as well as temporally (k). The second set of equations state that in each snapshot k, the ratio of total hydrogen vs. total yttrium should correspond to the known global composition $C = 1.39$, which is constant throughout all the snapshots k.

For this above system, the number of unknowns is $kN + 1$, where N is the number of hydrogen unknowns per snapshot times k snapshots, plus one yttrium unknown areal concentration, $n(Y)$. The number of equations is $kN + k$, where there are kN equations coming from the N pixels in each of the k snapshots and k equations from the known concentration at each snapshot. Because this is an over-determined system, we use a regularized, least-squares solution method where we seek the solution with minimum l_2-norm. This also allows us to introduce another regularization: since the areal concentrations for hydrogen and yttrium should be positive, we penalize solutions that are not positive. The trade-off between both regularizations is given by a constant lambda $>$ 0. Hence, the problem to solve corresponds to,

$$\min_{x} \|Ax - b\|^2 + \lambda\chi_P(x). \tag{5}$$

Here, the regularization rate is positive, $\lambda > 0$, and $\chi_P(x)$ is the characteristic function for set $P = \{x|x > 0\}$, defined as $\chi_P(x) := 0$ if $x \in P$, and $\chi_P(x) := \infty$ if $x \notin P$. Finally, A and b are matrices that can be written as,

$$A = \begin{bmatrix} A_1 & 0 & \cdots & 0 & 0 \\ 1 & 0 & \cdots & 0 & -NC \\ 0 & A_2 & \cdots & 0 & 0 \\ 0 & 1 & \cdots & 0 & -NC \\ \vdots & \vdots & \vdots & \vdots & \vdots \\ 0 & \cdots & 0 & A_K & 0 \\ 0 & \cdots & 0 & 1 & -NC \end{bmatrix} \text{ and } b = \begin{bmatrix} b_1 \\ 0 \\ b_2 \\ 0 \\ \vdots \\ b_K \\ 0 \end{bmatrix}. \tag{6}$$

Here, individual A and b matrices for each snapshot, k, are taken as,

$$A_k = \begin{bmatrix} \sigma_H & 0 & \cdots & 0 \\ \vdots & \ddots & \ldots & \ldots \\ 0 & \cdots & 0 & \sigma_H \end{bmatrix} \text{ and } b_k = \begin{bmatrix} p_{11} \\ \vdots \end{bmatrix}, \tag{7}$$

where, p_{11}, is the very first pixel in snapshot k.

We set lambda = 1e-4 and used the Scientific Computational Imaging Code (SCICO) [26] - a publicly available LANL Python software - to solve the regularized least-squares minimization. Some post-processed results are shown Fig. A-2. Here, the evolution of the average vertical YH_x composition, in red for the top pellet and in blue for the bottom pellet, is plotted as a function of temperature. Initial observations point to more inhomogeneous distributions within both pellets

and where the bottom pellet had an initial average composition of $YH_{1.6}$ while the top pellet was closer to $YH_{1.2}$. While the inhomogeneity was also observed in the room temperature images, the as-determined average stoichiometries from this analysis required further investigation. Additionally, it can be seen that hydrogen distributions within the top and bottom pellet seemed to reach equilibrium (within the samples and between each other) around 800°C with an approximate average stoichiometry of $YH_{1.4}$. Furthermore, as temperatures increased, there appeared to be a vertical downward gradient towards a higher stoichiometry across the pellets, this points to the possibility of unintended cooling at the bottom of the TZM can.

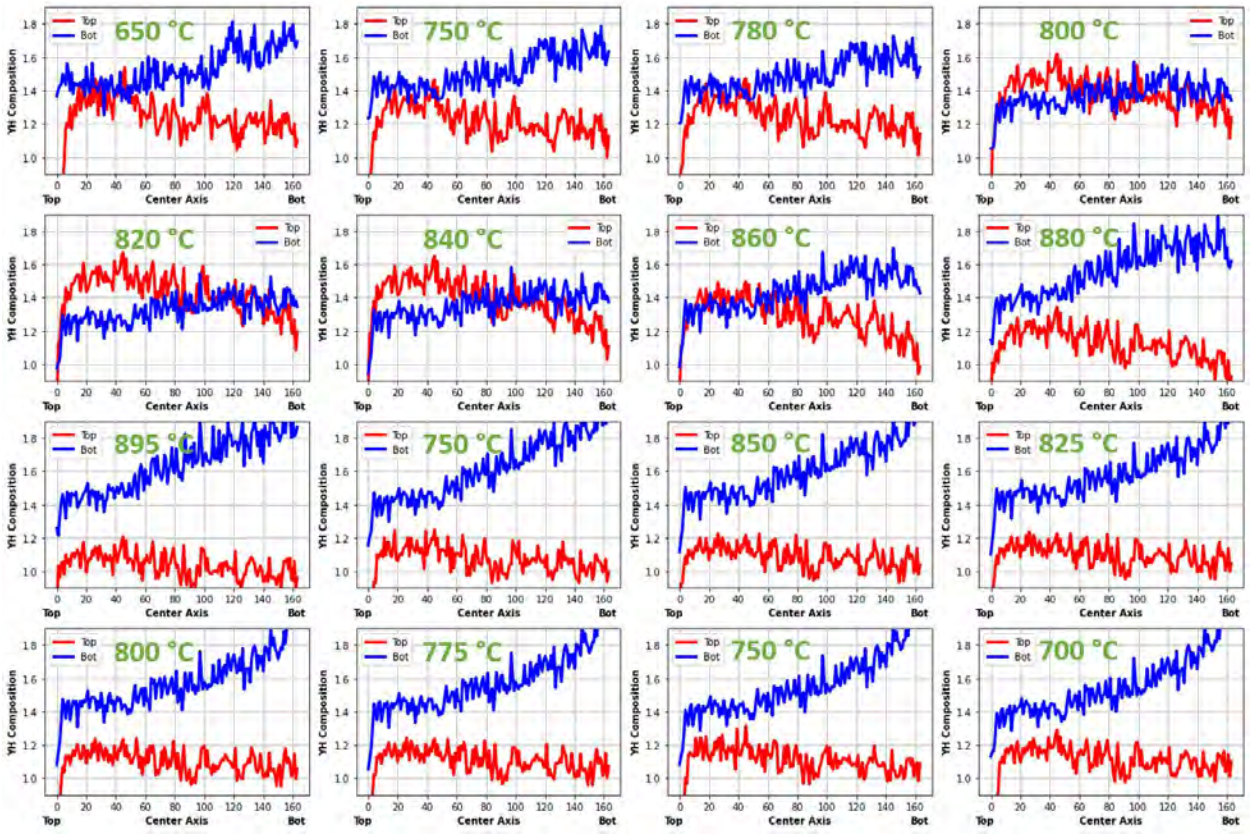

Figure A-2: Average vertical YH_x composition for top ($YH_{1.15}$) and ($YH_{1.63}$) as a function of applied temperatures. The top sample is plotted in blue and the bottom sample is plotted in red. Applied temperatures for each plot are given in green.

This type of analysis method was a novel application for modeling the relationship between neutron attenuation and hydrogen concentration with promising results. Further work is planned to refine the physics modeling with empirical parameters to the regularized least-squares minimization process.

Appendix B: Neutron Diffraction Measurements on YH

Neutron diffraction was conducted at the Los Alamos Neutron Science Center (LANSCE) using the High-Pressure-Preferred Orientation (HIPPO) diffractometer [27, 28]. Samples were loaded in vanadium cans to minimize the diffraction signal from sample holders. Diffraction data were acquired from five groups of detector panels at nominal diffraction angles of 2θ = 144°, 120°, 90°, 60°, and 39°. To increase pole figure coverage, measurements were taken for different rotations around the sample holder axis by 0°, 67.5° and 90° with respect to the beam. A Rietveld refinement employing the Material-Analysis-Using-Diffraction (MAUD) program [29] was performed against the resulting 135 neutron diffraction patterns per sample using the E-WIMV method with a 7.5° resolution in order to simultaneously fit all of the diffraction data and determine the orientation distribution function (ODF) of the phases (YH_2 with the fluorite crystal structure and α-Y with a hexagonal closed packed crystal structure) of each sample.

To investigate the decomposition of YH2, a yttrium hydride pellet designated "M112221C" was heated in the HIPPO ILL furnace [28] from room temperature to 850°C. The sample was contained in a vanadium can. Starting with initial measurements at room temperature, subsequent measurements were taken at 150°C, 200°C, 300°C, 450°C, 600°C, 700°C, with each measurement taking on the order of several minutes. Once at 700°C continuous data was collected during temperature ramping up to 850°C at 1C/min, followed by a one hour hold at 850°C.Additionally, data was also collected during cooling. Two thermocouples recorded the temperature. The 300 diffraction patterns were analyzed using the Rietveld method using the GSAS software package [30] automated by the GSAS-language script language [31]

B.1 Results of Ambient Texture Measurements on HIPPO

Sample 157-1 consists mostly of αY (94.1 wt%), indicating per Y-H phase diagram a H/Y ratio of <0.5. Remarkably, the texture of the αY is similar to a single crystal, meaning the probed volume, essentially the entire pellet, is one large crystal of α-Y. This would in turn indicate that grain boundaries etc. are largely absent, affecting the hydriding process of such a microstructure. This is further illustrated in analyzed pole figures shown in Fig. B-1.

Sample 176-1 has no detectable α-Y phase present, which per phase diagram indicates a H/Y ratio >1.9. Furthermore, there is no detectable preferred orientation in the YH2 phase. If the original metallic yttrium cylinder used to prepare this sample has a similarly strong texture or preferred orientation as the previous sample, this would be an indication that during the hydriding process the texture is randomized.

B.2 Results of Heating Texture Measurements on HIPPO

In 2019 experiments were conducted with the same setup but characterizing powders of sub-stoichiometric YH_{2-x} (1.48, 1.81 and 1.92) and different temperature profile with holds at 750°C, 775°C, 800°C, 825°C, 850°C for approximately 3 hours each (8 times 20 minutes). In 2019, we saw decomposition of all of the measured YH_{2-x} samples around 800°C with a dependence of decomposition temperature on the x. The goal of the current continuous heating with 1°C/min was to determine the decomposition temperature more accurately over the 25°C steps from 2019. In the current runs, at the end of the 850°C hold there is still no detectable α-Y. There is detectable Y during cooling, with clear diffraction peaks. The weight fraction refines to 40 wt.%) during cooling.

Appendix B: Neutron Diffraction Measurements on YH

This result is somewhat surprising since all samples in 2019 were decomposed to pure α-Y at 850°C. Analysis of this experiment is still on-going.

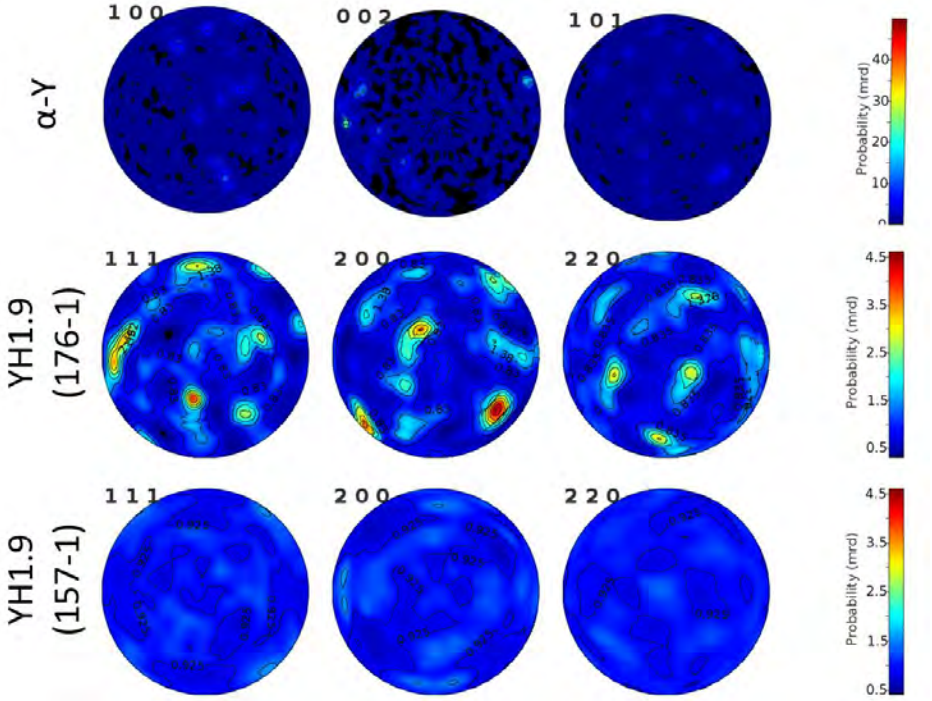

Figure B-1: Pole figures of α-Y (top), $YH_{1.9}$ "157-1" (middle), and $YH_{1.9}$ "176-1" (bottom) as received from FP5. The sample cylinder axis (pellet axis) is in the center of the pole figure. Note the different scales for the pole figures of the two phases between α-Y and $YH_{1.9}$ (given in multiples of random distribution).

References

[1] Holly Renee Trellue et al. *Microreactor Demonstration and Testing Progress in FY19*. Tech. rep. Los Alamos, NM (United States): Los Alamos National Laboratory (LANL), 2019. DOI: 10.2172/1566087. URL: https://www.osti.gov/servlets/purl/1566087/https://www.osti.gov/servlets/purl/1566087%0Ahttps://www.osti.gov/biblio/1566087.

[2] Aditya Shivprasad et al. *Advanced Moderator Material Handbook*. Tech. rep. Los Alamos, NM (United States): Los Alamos National Laboratory (LANL), 2020. DOI: 10.2172/1671020. URL: https://www.osti.gov/servlets/purl/1671020/.

[3] Vedant Mehta, Patrick McClure, and Dan Kotlyar. "Selection of a space reactor moderator using lessons learned from snap and anp programs". In: *AIAA Propulsion and Energy Forum and Exposition, 2019*. Reston, Virginia: American Institute of Aeronautics and Astronautics, 2019. ISBN: 9781624105906. DOI: 10.2514/6.2019-4451. URL: https://arc.aiaa.org/doi/10.2514/6.2019-4451.

[4] Vedant K. Mehta et al. "Capturing multiphysics effects in hydride moderated microreactors using MARM". In: *Annals of Nuclear Energy* 172 (2022), p. 109067. ISSN: 18732100. DOI: 10.1016/j.anucene.2022.109067.

[5] Christopher Matthews, Aditya Shivprasad, and Michael Cooper. *Metal Hydride Simulations Using SWIFT*. Tech. rep. Los Alamos, NM (United States): Los Alamos National Laboratory (LANL), 2021. DOI: 10.2172/1829624. URL: https://www.osti.gov/servlets/purl/1829624/.

[6] H. H. Klepfer, H. D. Kosanke, and E. L. Esch. "Neutrographic Hydrogen Determination in Zirconium Alloys". In: *Applications-Related Phenomena in Zirconium and its Alloys*. ASTM International, 1968, pp. 372–372–14. DOI: 10.1520/STP43840S. URL: http://www.astm.org/doiLink.cgi?STP43840S.

[7] M. Zanarini et al. "Evaluation of Hydrogen content in Metallic Samples by Neutron Computed Tomography". In: *IEEE Transactions on Nuclear Science* 42.4 (1995), pp. 580–584. ISSN: 15581578. DOI: 10.1109/23.467910. URL: https://ieeexplore.ieee.org/document/467910/.

[8] Ryou Yasuda et al. "Application of neutron radiography for estimating concentration and distribution of hydrogen in Zircaloy cladding tubes". In: *Journal of Nuclear Materials* 302.2-3 (2002), pp. 156–164. ISSN: 00223115. DOI: 10.1016/S0022-3115(02)00778-X.

[9] Ryou Yasuda et al. "Application of hydrogen analysis by neutron imaging plate method to Zircaloy cladding tubes". In: *Journal of Nuclear Materials* 320.3 (2003), pp. 223–230. ISSN: 00223115. DOI: 10.1016/S0022-3115(03)00112-0. URL: https://www.sciencedirect.com/science/article/pii/S0022311503001120.

[10] W. Gong et al. "Hydrogen diffusion and precipitation in duplex zirconium nuclear fuel cladding quantified by high-resolution neutron imaging". In: *Journal of Nuclear Materials* 526 (2019). ISSN: 00223115. DOI: 10.1016/j.jnucmat.2019.151757. URL: https://www.sciencedirect.com/science/article/pii/S0022311519303101.

References

[11] Tyler Smith et al. "High Resolution Neutron Radiography and Tomography of Hydrided Zircaloy-4 Cladding Materials". In: *Physics Procedia* 69.October 2014 (2015), pp. 478–482. ISSN: 18753892. DOI: 10.1016/j.phpro.2015.07.067. URL: http://dx.doi.org/10.1016/j.phpro.2015.07.067.

[12] M. Grosse et al. "Quantitative determination of absorbed hydrogen in oxidised zircaloy by means of neutron radiography". In: *Nuclear Instruments and Methods in Physics Research, Section A: Accelerators, Spectrometers, Detectors and Associated Equipment* 566.2 (2006), pp. 739–745. ISSN: 01689002. DOI: 10.1016/j.nima.2006.06.038.

[13] M. Grosse et al. "In-situ neutron radiography investigations of hydrogen diffusion and absorption in zirconium alloys". In: *Nuclear Instruments and Methods in Physics Research, Section A: Accelerators, Spectrometers, Detectors and Associated Equipment* 651.1 (2011), pp. 253–257. ISSN: 01689002. DOI: 10.1016/j.nima.2010.12.070. URL: http://dx.doi.org/10.1016/j.nima.2010.12.070.

[14] Xunxiang Hu et al. "Fabrication of yttrium hydride for high-temperature moderator application". In: *Journal of Nuclear Materials* 539 (2020), p. 152335. ISSN: 00223115. DOI: 10.1016/j.jnucmat.2020.152335.

[15] A. P. Shivprasad et al. "Elastic moduli of high-density, sintered monoliths of yttrium dihydride". In: *Journal of Alloys and Compounds* 826 (2020), p. 153955. ISSN: 09258388. DOI: 10.1016/j.jallcom.2020.153955.

[16] M. Mocko, G. Muhrer, and F. Tovesson. "Advantages and limitations of nuclear physics experiments at an ISIS-class spallation neutron source". In: *Nuclear Instruments and Methods in Physics Research, Section A: Accelerators, Spectrometers, Detectors and Associated Equipment* 589.3 (2008), pp. 455–464. ISSN: 01689002. DOI: 10.1016/j.nima.2008.02.100.

[17] M. Mocko and G. Muhrer. "Fourth-generation spallation neutron target-moderator-reflector-shield assembly at the Manuel Lujan Jr. neutron scattering center". In: *Nuclear Instruments and Methods in Physics Research, Section A: Accelerators, Spectrometers, Detectors and Associated Equipment* 704 (2013), pp. 27–35. ISSN: 01689002. DOI: 10.1016/j.nima.2012.11.103. URL: https://www.sciencedirect.com/science/article/pii/S0168900212014507.

[18] Ronald O. Nelson et al. "Neutron imaging at LANSCE—from cold to ultrafast". In: *Journal of Imaging* 4.2 (2018), pp. 1–26. ISSN: 2313433X. DOI: 10.3390/jimaging4020045. URL: https://www.mdpi.com/2313-433X/4/2/45.

[19] Anton S. Tremsin et al. "HIgh Resolution Photon Counting With MCP-Timepix Quad Parallel Readout Operating at 1 KHz Frame Rates". In: *IEEE Transactions on Nuclear Science* 60.2 (2013), pp. 578–585. ISSN: 00189499. DOI: 10.1109/TNS.2012.2223714. URL: https://ieeexplore.ieee.org/document/6375792.

[20] Anton S. Tremsin, W. Bruce Feller, and R. Gregory Downing. "Efficiency optimization of microchannel plate (MCP) neutron imaging detectors. I. Square channels with 10B doping". In: *Nuclear Instruments and Methods in Physics Research, Section A: Accelerators, Spectrometers, Detectors and Associated Equipment* 539.1-2 (2005), pp. 278–311. ISSN: 01689002. DOI: 10.1016/j.nima.2004.09.028.

[21] Leo R. Dalesio et al. "The experimental physics and industrial control system architecture: past, present, and future". In: *Nuclear Inst. and Methods in Physics Research, A* 352.1-2 (1994), pp. 179–184. ISSN: 01689002. DOI: 10.1016/0168-9002(94)91493-1.

References

[22] Anders P. Kaestner. "MuhRec—A new tomography reconstructor". In: *Nuclear Instruments and Methods in Physics Research Section A: Accelerators, Spectrometers, Detectors and Associated Equipment* 651.1 (2011), pp. 156–160. ISSN: 01689002. DOI: 10.1016/j.nima.2011.01.129. URL: https://linkinghub.elsevier.com/retrieve/pii/S0168900211002312.

[23] James Ahrens, Berk Geveci, and Charles Law. "ParaView: An end-user tool for large-data visualization". In: *Visualization Handbook*. Elsevier, 2005, pp. 717–731. ISBN: 9780123875822. DOI: 10.1016/B978-012387582-2/50038-1. URL: https://linkinghub.elsevier.com/retrieve/pii/B9780123875822500381.

[24] J. Eric Lynn, Walter J. Trela, and Kai Meggers. "Neutron Doppler broadening studies of tantalum and tungsten metal". In: *Nuclear Instruments and Methods in Physics Research, Section B: Beam Interactions with Materials and Atoms* 192.3 (2002), pp. 318–330. ISSN: 0168583X. DOI: 10.1016/S0168-583X(02)00480-9.

[25] A. S. Tremsin et al. "Spatially resolved remote measurement of temperature by neutron resonance absorption". In: *Nuclear Instruments and Methods in Physics Research, Section A: Accelerators, Spectrometers, Detectors and Associated Equipment* 803 (2015), pp. 15–23. ISSN: 01689002. DOI: 10.1016/j.nima.2015.09.008. URL: http://dx.doi.org/10.1016/j.nima.2015.09.008.

[26] Thilo Balke et al. *Scientific Computational Imaging COde (SCICO)*. Software library available from https://github.com/lanl/scico. 2022.

[27] H. R. Wenk, L. Lutterotti, and S. Vogel. "Texture analysis with the new HIPPO TOF diffractometer". In: *Nuclear Instruments and Methods in Physics Research, Section A: Accelerators, Spectrometers, Detectors and Associated Equipment* 515.3 (2003), pp. 575–588. ISSN: 01689002. DOI: 10.1016/j.nima.2003.05.001.

[28] Sven C. Vogel et al. "Texture measurements using the new neutron diffractometer HIPPO and their analysis using the Rietveld method". In: *Powder Diffraction* 19.1 (2004), pp. 65–68. ISSN: 0885-7156. DOI: 10.1154/1.1649961. URL: https://www.cambridge.org/core/product/identifier/S0885715600008691/type/journal_article.

[29] H.-R. Wenk, L. Lutterotti, and S. C. Vogel. "Rietveld texture analysis from TOF neutron diffraction data". In: *Powder Diffraction* 25.3 (2010), pp. 283–296. ISSN: 0885-7156. DOI: 10.1154/1.3479004. URL: https://www.cambridge.org/core/product/identifier/S0885715600000324/type/journal_article.

[30] Allen C. Larson and Robert B. Von Dreele. *GSAS: General Structure Analysis System*. Tech. rep. Los Alamos, NM: Los Alamos National Laboratory, 2000. URL: https://11bm.xray.aps.anl.gov/documents/GSASManual.pdf.

[31] Sven C. Vogel. "Gsaslanguage: A GSAS script language for automated Rietveld refinements of diffraction data". In: *Journal of Applied Crystallography* 44.4 (2011), pp. 873–877. ISSN: 00218898. DOI: 10.1107/S0021889811023181. URL: http://scripts.iucr.org/cgi-bin/paper?S0021889811023181.